High Fidelity CFD/CSD Method for Rotor Blade Optimisation

Mark A. Woodgate
University of Glasgow
Glasgow, United Kingdom

George N. Barakos
University of Glasgow
Glasgow, United Kingdom

ABSTRACT

This paper introduces an innovative framework that leverages high-fidelity methods to design rotor blades, which aerospace engineers can use to improve overall airframe performance. A generalised blade surface parameterisation, which includes variations in twist, chord, sweep and anhedral, is applied to an initial rectangular blade to maintain a given thrust and reduce torque levels. Emphasis is placed on coupling aeroelasticity with the adjoint optimisation and trimming methods at desired flight conditions. Conclusions include the effect of including aeroelasticity in a sample blade design, and a discussion of the optimisation framework.

NOTATION

*

Symbols

α Design Paramter

ζ Structural Damping

*

Acronyms

ERF European Rotorcraft Forum

BILU Block Incomplete Lower-Upper

CFD Computational Fluid Dynamics

CSD Computational Structural Dynamics

HMB3 Helicopter Multi Block 3

IDW Inverse Distance Weighting

MLS Moving Least Squares

MUSCL Monotone Upstream-centred Scheme for Conservation Laws

SST Shear Stress Transport

INTRODUCTION

Improved designs of helicopter rotor blades aim to reduce fuel consumption, expand flight envelopes, and minimise noise and vibration. Achieving this requires careful consideration of the blade shape to meet design objectives while accounting for practical constraints.

In recent years, there has been evidence of at least some use of optimisation in real-world blade designs. Advanced planform shapes such as the BERP design (Ref. 1), the Blue-Edge blade (Ref. 2) or the Advanced Chinook Rotor Blade (ACRB) (Ref. 3) show that rotor design is still progressing, and there is mileage to cover before each helicopter's most optimal blade shape can be delivered. Looking at these works, the development of the BERP blade used experiments on scaled rotors with Computational Fluid Dynamics (CFD) only being used towards the end of its development. The BlueEdge final design was achieved after several stages and iterations supported by various research projects and extensive experimentation. The ACRB blade is a more recent development, and its design relied more on numerical simulations and CFD. However, during initial testing vibration and a stall on the aft rotor were reported.

Looking forward, the future of rotor design lies in high-fidelity models coupled with optimisation methods. The broader literature shows two main lines of research related to gradient-free and gradient-based optimisation methods. The overall understanding is that gradient-free methods need more CFD computations to deliver the optimum. In contrast, the gradient-based methods need more effort to develop, and unless care is taken, they may lead to local optima near the starting blade design.

Gradient-free methods are prevalent because they are relatively easy to develop and implement using existing computer codes. For example, any CFD solver capable of computing rotor flows can be used with some form of meta-model to "curve-fit" the predicted aerodynamics, and feed it to a mesh generation tool and an optimisation method. The most popular meta-models include Kriging, rational basis functions, neural networks, and simple look-up tables. If the meta-model is heavily populated with CFD results for different designs, gradients of the aerodynamics with respect to the design parameters can also be computed, leading to a gradient-based method. As the number of design parameters increases to allow for more complex blade shapes, the number of required CFD computations becomes high, and such methods are of little practical use.

On the other hand, gradient-based methods require fewer CFD computations and may scale better with the number of design variables. Compared to parametric studies, gradient-based optimisation methods allow the exploration of a more comprehensive design space and better support the designer in selecting the optimal shape of the blade. They also allow for the exploration of more novel blade designs and provide insight into the effect of design characteristics on the final aerodynamics. On the other hand, such advanced methods rely upon algorithmic advancements in terms of solution fidelity, accuracy, computational costs, and coupling of multidisciplinary analyses (including aerodynamics, aeroelasticity, structures, vibration, and noise). Capturing the multidisciplinary aspects of rotor design is vital for industrial use as it ensures realistic designs are obtained. Finally, choosing the optimisation method and design parameters will also drive the design changes, impacting the final result. Future rotor design is likely to be performed adaptively without pre-set parameters based on engineering judgment. A comprehensive literature on rotor blade design can be found in (Ref. 4).

METHODOLOGY

This section describes the CFD-CSD methodology used in the present work. This includes the HMB3 solver, the harmonic balance method, the adjoint method, the optimisation framework, the middleware tool which interfaces HMB3 with NASTRAN, the blade parameterisation and design framework, and the blade Structural model.

CFD Solver

The Helicopter Multi-Block 3 (HMB3) toolset is, an in-house development that is used for all simulations in this work. The computational fluid dynamics tool is a finite volume solver on structured multi-block grids (Ref. 5) with an overset grid method (Ref. 6). HMB3 solves the Unsteady Reynolds Averaged Navier-Stokes (URANS) equations in integral form using the Arbitrary Lagrangian Eulerian (ALE) formulation for time-dependent domains, including moving boundaries.

The two different solution formulations applied within this work are shown in equations 1-2.

$$\frac{d\mathbf{W}}{dt} + \mathbf{R}(\mathbf{W}) = \mathbf{S} \qquad \text{Steady} \qquad (1)$$

$$\frac{d\mathbf{W}_{hb}}{dt} + \omega D\mathbf{W}_{hb} + \mathbf{R}_{hb}(\mathbf{W}) = 0 \qquad \text{HB} \qquad (2)$$

where, $\mathbf{W}$ is the vector of conserved variables, $\mathbf{R}$ is the residual vector, $\mathbf{S}$ is the source term, t is the real time step, ω is the reduced frequency, D is the Fourier collocation derivative operator and HB (and hb) refers to the Harmonic Balance method.

For both methods, to evaluate the convective fluxes, the Osher (Ref. 7) approximate Riemann solver is used, while the viscous terms are discretised using a second-order central differencing spatial scheme. The MUSCL approach developed by Leer (Ref. 8) is used to provide high-order accuracy in space with the alternative form of the Albada limiter (Ref. 9) in regions of large gradients. The implicit, dual-time stepping method of Jameson is employed. The linearised system of equations is solved using the Generalised Conjugate Gradient method with a BILU factorisation as a pre-conditioner. One-equation to four-equation turbulence models are available in the HMB3 solver, and the 1994 k-ω SST model of Menter (Ref. 10) was used for the computations presented in this paper.

The hover out-of-ground effect (OGE) simulations in HMB3 use the Froude boundary condition. The rotor mesh consists of $2\pi/N_b$ of the rotor domain, with N_b the total number of blades. Consequently, this mesh contains only one blade, which is sufficient for hover calculations with periodic boundary conditions when using a steady state formulation. A source term is added to the discretised Navier-Stokes equations to take account of the rotational velocity component of the rotor.

To reduce the computational costs associated with unsteady adjoint-based designs, the harmonic balance method (Refs. 11–14) is used for forward flight cases. This method treats the solution as a large, steady problem by assuming periodicity in time, with an additional unsteady source term. The steady nature of the solution procedure makes that attractive for adjoint optimisation studies, as the steady adjoint solver (with certain modifications) can be used.

The harmonic balance method represents the flow solution and residual vectors as a truncated Fourier series, by assuming periodicity in time with frequency, ω. The flow is represented by N_H harmonic balance modes and is split into $N_T = 2N_H + 1$ subintervals, which are coupled using the Fourier collocation derivative operator, D. This leads to a significant reduction in computational costs compared to time-marching simulations, as the flow-field can be solved as a large ($N_T \times N_T$) steady state problem.

Adjoint Method

The adjoint method offers an efficient way to produce the gradients of the design variables, which are used in conjunction with a gradient-based optimiser. Compared to finite differences, where the gradient computation is dependent on the number of variables, the adjoint method generates the gradients of all the design variables at the cost of a base flow solution.

Consider a cost function I which needs to be optimised as a function of the design parameters α

$$\frac{\mathrm{d}I}{\mathrm{d}\alpha} = \frac{\partial I}{\partial \alpha} + \frac{\partial I}{\partial \mathbf{W}}\frac{\partial \mathbf{W}}{\partial \alpha}. \tag{3}$$

By introducing the adjoint variable λ equation (3) can be rewritten as

$$\frac{\mathrm{d}I}{\mathrm{d}\alpha} = \frac{\partial I}{\partial \alpha} + \lambda^{\mathrm{T}}\frac{\partial \mathbf{R}}{\partial \alpha}. \tag{4}$$

For the sensitivities of the design variables, the term $\frac{\partial \mathbf{R}}{\partial \alpha}$ is obtained using the chain rule:

$$\frac{\partial \mathbf{R}}{\partial \alpha} = \frac{\partial \mathbf{R}}{\partial \mathbf{N}}\frac{\partial \mathbf{N}}{\partial \mathbf{X}_v}\frac{\partial \mathbf{X}_v}{\partial \mathbf{X}_s}\frac{\partial \mathbf{X}_s}{\partial \alpha} \tag{5}$$

This represents the computation of the residual vector sensitivities with respect to the design variables, and is dependent on the surface mesh sensitivities with respect to each design variable $\partial \mathbf{X}_s/\partial \alpha$ which are obtained from the blade parameterisation, the volume mesh sensitivities with respect to the surface mesh $\partial \mathbf{X}_v/\partial \mathbf{X}_s$, the mesh metrics sensitivities with respect to the volume mesh $\partial \mathbf{N}/\partial \mathbf{X}_v$ and finally, the residual sensitivities with respect to the mesh metrics $\partial \mathbf{R}/\partial \mathbf{N}$.

The adjoint method was developed within HMB3 through source code differentiation, using the tool TAPENADE (Ref. 15) and the validation, and verification of the present adjoint method has been detailed in earlier publications, e.g. (Ref. 16).

Static Aeroelasticity

The hover (OGE) simulations use a steady formulation and hence only the static loading of the aerodynamic and angular velocity is required for a converged aeroelastic simulation. Figure 1 shows how HMB3 and MSC/NASTRAN communicate through the communication interface or middleware. The middleware processes the flow data from HMB3 to generate the aerodynamic loads used in MSC/NASTRAN and then uses a system call to start the analysis. Once MSC/NASTRAN has finished the middleware processes, the results - nodal displacements and eigenmodes - and interpolates them onto the HMB3 surface mesh and communicates them to HMB3.

The moving least squares method (Ref. 17) is used for smoothing and interpolating data between the CFD and CSD grids. The method starts with a weighted least squares formulation for an arbitrary fixed point in space. Then, it moves this point over the entire parameter domain, where a weighted least squares fit is computed and evaluated for each point individually. The volume grid is then deformed using the Inverse Distance Weighting (IDW) method proposed by Luke et al. (Ref. 18). IDW is a multivariate interpolation method that calculates the value at an unknown point with a weighted average of the values of a known set of scattered points. The weight assigned to the value at a known point is proportional to the inverse distance between the known and the unknown point.

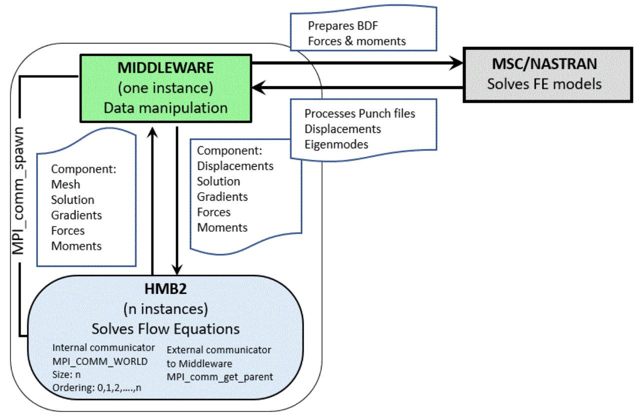

Figure 1. Using the middleware to couple HMB3 to MSC/NASTRAN

Dynamic Aeroelasticity

The modal analysis of the aero-elastic system begins with a set of equations that describe its behaviour. These equations have the general form:

$$[M]\ddot{U}(t) + [C]\dot{U}(t) + [K]U(t) = F(t) \tag{6}$$

where $[K]$, $[C]$ and $[M]$ are the stiffness, damping, and mass matrices of the system while $U(t)$ and $F(t)$ are the vector of generalised displacements and forces at time t. In the modal method the displacement vector $U(t)$ is then restricted to a subset of all possible displacements by allowing the first m mode shapes each with an scale factor.

$$U(t) = sum_{i=1}^{m}\phi_i \cdot \alpha_i(t) = [\Phi]A(t) \tag{7}$$

where ϕ_i is the ith mode shape and $\alpha_i(t)$ is the ith scaling factor at time t. Since the modal matrix $[\Phi]$ is independent of time equation 7 and be substituted into 6 and premultiplying by $[\Phi]^T$,

$$[M_m]\ddot{A}(t) + [C_m]\dot{A}(t) + [K_m]A(t) = [\Phi]^T F(t) \tag{8}$$

where $[M_m] = [\Phi]^T M[\Phi]$, $[C_m] = [\Phi]^T C[\Phi]$, and $[K_m] = [\Phi]^T K[\Phi]$. The mode shapes are then scaled so that the modal mass matrix becomes the identity matrix $[I]$ and the modal stiff matrix becomes a diagonal matrix with the entries equal to the square of the mode shapes natural frequency ω_i. Assuming the damping of each mode is proportional to the critical damping for that mode then equation 8 becomes

$$\ddot{\alpha}_i(t) + 2\zeta_i\omega_i\dot{\alpha}_i(t) + \omega_i^2\alpha_i(t) = [\Phi]^T F(t) \tag{9}$$

where ζ_i are the structural damping coefficients. The α_i then can be calculated independently and combined by linear superposition using equation 7 to obtain the displacement vector.

In this work the modal equation 9 is also solved by the harmonic balance formulation with the assumption that the $\alpha_i(t)$ scaling factors are also periodic with the same frequency as the flow variables. This results in the time derivatives of equation 9 begin replaced by their harmonic balance counterparts resulting in the equation

$$\left(\omega_{HB}^2[D]^2 + \omega_{HB}[D]\dot{\zeta}_i\omega_i + \omega_i^2\right)\alpha_i = [\Phi]^T F \qquad (10)$$

The solution of the modal equation is linear with the size of the number of harmonic balance snapshots. The linear system is solved for each solid surface and structural mode to obtain the modal amplitudes. The linear system is solved using Gaussian elimination. As the equation is solved in dimensional units (modal frequencies in rad/s), the harmonic balance frequency also needs to be converted from a reduced frequency to the angular frequency of the rotor.

Finite Element Model

In this work, beam finite element models are used. Given the difficulty in obtaining the structural design and properties an approximate dynamic model will be used based on the published parameters of AH-64A blade. The model was developed in NASTRAN with the resultant modal frequencies compared with other computational work and experimental data. For the 1D beam model, a similar approach to (Ref. 19) is followed here. The blade is discretised using CBEAM elements with rigid bar elements (RBAR) used to visualise and map the torsion of the beam to the CFD mesh. For the base line blade, the blade structure is discretised using 39 CBEAM elements along the blade span as shown in Figure 2.

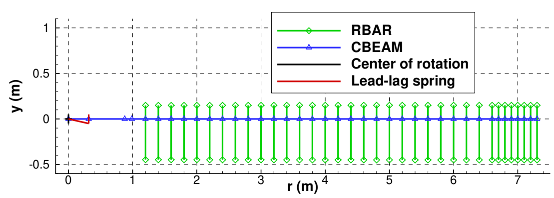

Figure 2. Structural 1D beam model for the base line rotor blade

Including aeroelastic effects in blade optimisation requires adapting the blade's structural model to account for changes in shape. Certain optimisation studies include aeroelastic effects but do not update the structural model during the optimisation study (Refs. 20, 21), which may lead to inaccuracies for example in the torsional deformations for blades with high variations in sweep along the span. For this reason, even though the structural properties are not optimised, they are adapted to changes in blade shape. In this work, we follow the approach of Stanger (Ref. 22), which was also used by Wilke (Ref. 23). Adapting the structural properties is based on structural scaling laws with rotor blade chord and sweep changes. Monocoque scaling was used here, which assumes that the blade skin thickness is kept constant and that only the internal structure is scaled. This scaling leads to linear scaling in moments of inertia and third-order scaling in stiffnesses. The effect of sweep modifies the location of the elastic axis along the blade span, whereas twist rotates the local beam element axis. The changes in anhedral/dihedral are neglected. Table 1 shows the applied scaling factors.

Property	Scaling Factor
Mass	α
Area	α
Polar moment of inertia	α
Torsional Stiffness	α^3
Flapwise Stiffness	α^3
Chordwise Stiffness	α^3

Table 1. Structural property scaling factors applied with changes in blade shape. $\alpha = c_{new}/c_{ref}$ **(Ref. 22).**

Blade Surface Parameterisation

The rotor blade uses a surface parameterisation to deform its shape. In this case, the parameterisation of the baseline blade is composed of twist, chord sweep and anhedral design variables. Different combinations of the design variables result in a range of blade designs as shown in figure 3. A Bernstein polynomial function with seven coefficients changes the

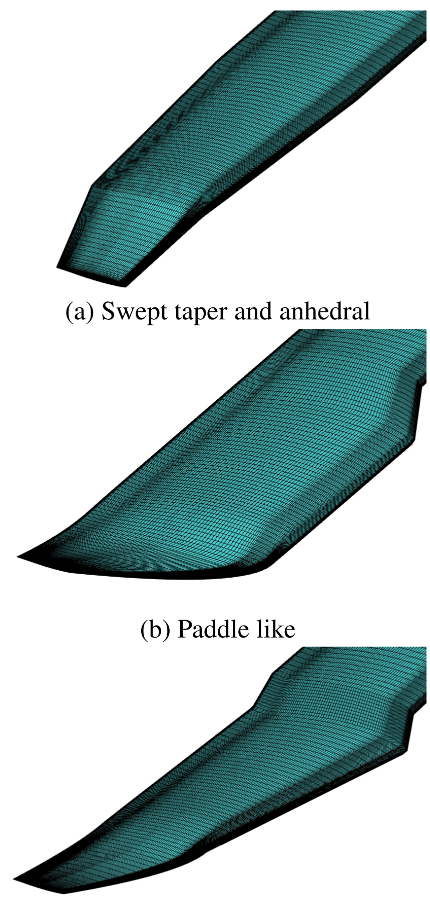

(a) Swept taper and anhedral

(b) Paddle like

(c) Blue Edge like tip (non planar)

Figure 3. Some of the possible tip shape designs

blade twist while the chord, sweep and anhedral are varied at any number of prescribed radial stations along the blade. In this example, no variation is allowed at the first radial station, and the blade root. All blade sections allow for linear variations of the design parameters, except for the blade section between the penultimate and last radial stations, which can be either linear or parabolic. The current example uses eight chord, seven sweep, and anhedral stations (see figure 4). Adding more stations and more design parameters expands

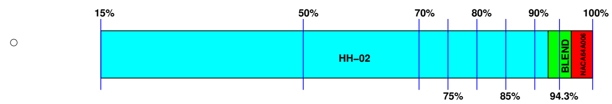

Figure 4. Example of control station distribution along the blade radius.

the family of shapes produced, and given that the current work uses an adjoint formulation, the penalty is mainly in the complexity of the shapes and the analysis of the reasons behind each design change rather than in CPU time. Smoothing of the surface can be applied at each design stage to guarantee high-order continuity between the parameterisation stations. There is enough flexibility to capture several blade tip shapes, even with the 29 design variables used in this example.

Table 2. Design parameter upper and lower boundaries for optimisation studies of the AH-64A blade.

Design Parameter	Boundary values
TWIST1 - TWIST7	± 6 deg
CHORD at r/R = 0.5	[0.8c,1.2c]
CHORD at r/R = 0.70	[0.8c,1.4c]
CHORD at r/R = 0.75	[0.8c,1.4c]
CHORD at r/R = 0.80	[0.8c,1.4c]
CHORD at r/R = 0.85	[0.8c,1.4c]
CHORD at r/R = 0.90	[0.8c,1.4c]
CHORD at r/R = 0.943	[0.8c,1.4c]
CHORD at r/R = 1.0	[0.3c,1.4c]
SWEEP at r/R = 0.70	[-0.4c,0.4c]
SWEEP at r/R = 0.75	[-0.4c,0.4c]
SWEEP at r/R = 0.80	[-0.4c,0.4c]
SWEEP at r/R = 0.85	[-0.4c,0.4c]
SWEEP at r/R = 0.90	[-0.4c,0.4c]
SWEEP at r/R = 0.943	[-0.4c,0.4c]
SWEEP at r/R = 1.0	[-0.7c,0.4c]
ANHEDRAL at r/R = 0.70	[-0.1c,0.1c]
ANHEDRAL at r/R = 0.75	[-0.1c,0.1c]
ANHEDRAL at r/R = 0.80	[-0.1c,0.1c]
ANHEDRAL at r/R = 0.85	[-0.1c,0.1c]
ANHEDRAL at r/R = 0.90	[-0.1c,0.1c]
ANHEDRAL at r/R = 0.943	[-0.1c,0.1c]
ANHEDRAL at r/R = 1.0	[-0.2c,0.1c]

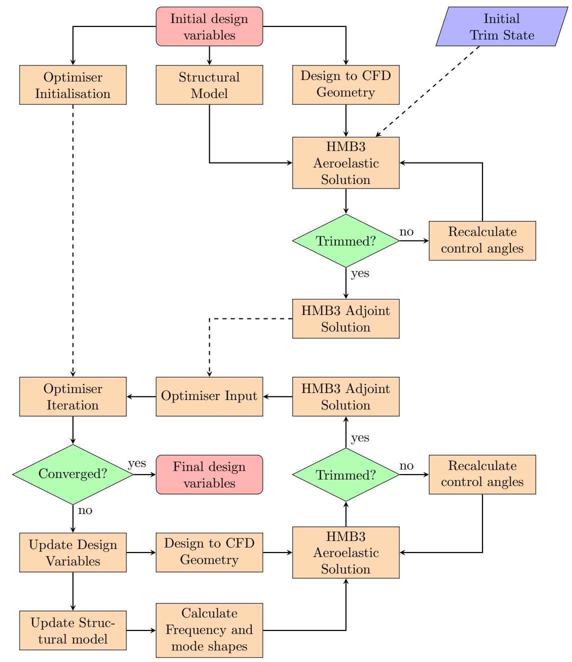

Figure 5. The HMB3 optimisation workflow.

Optimisation Framework

Figure 5 shows the workflow for the forward flight optimisation. The figure shows that aeroelasticity, blade trimming, and shape optimisation are the main blocks working together iteratively. Nevertheless, it is the parameterisation of the blade and the selection of the design aspects that the optimisation can alter, which captures the design philosophy of the engineer in charge. Firstly, the baseline flow solution is computed using the steady-state solver or the harmonic balance method. The baseline objective function and constraints are then evaluated from the base flow solution. The adjoint problem is then solved, and the design sensitivities are computed using the adjoint method. Typically, the adjoint problem is approximately solved to minimise computational costs. The main aim of the adjoint method is to provide gradients of sufficient accuracy to drive the design in the correct direction. The cost functional, constraints, and gradients are fed to the gradient-based optimiser to obtain a new design variable vector. Based on the new vector of design variables, the coordinates of the new surface and the surface sensitivities, which are used in the adjoint method, are generated. Finally, a mesh deformation algorithm based on Inverse-Distance Weighting is employed to update the volume mesh. The optimisation workflow continues until the objective function or design variables change reaches a set tolerance.

RESULTS AND DISCUSSIONS

Hover Aeroelastic

The rectangular blade was optimised in aeroelastic hover. This demonstrates the coupling of aeroelasticity with the adjoint methods even if the computation is performed here as a steady-state flow assuming spatial and temporal periodicity. This is like a zero mode optimisation. The optimisation is performed for an aeroelastic rotor and involves a power minimisation problem whilst constraining the thrust. The nominal rotor speed is set to 270 RPM, resulting in a tip Mach number of 0.606 and a tip Reynolds number of 8.74 million. Table shows the thrust, torque and figure of merit values for the baseline blade. The $C_T = 0.0085$ at the collective of 7.7 degrees, where the figure of merit starts decreasing, was chosen as the constraining thrust for the optimisation.

Collective	Thrust (N)	Torque (Nm)	FoM
4.0	41050	22930	0.632
5.0	51310	30150	0.671
6.0	61620	39060	0.682
7.0	69890	47670	0.675
8.0	78060	58230	0.652

Table 3. Effect of collective on the thrust torque and figure of Merit values for the base line blade.

At each step of the optimisation, the structural model is updated based on the new planform shape, and then an aeroelastic hover calculation is performed. Finally, a separate adjoint calculation is launched, with the aeroelastic deformation built into the grid. The optimisation process shows significant benefits after only three iterations, see figure , with the peak figure of Merit increasing to 0.789 for the aeroelastic hover-optimised blade.

Collective	Thrust (N)	Torque (Nm)	FoM
5.0	42548	24800	0.61
7.0	90740	60520	0.786
8.0	101300	71120	0.789
9.0	136300	120500	0.727

Table 4. Effect of collective on the thrust torque and figure of Merit values for the base line blade.

The hover optimised blade has 4% more mass and table 5 shows the small changes in eigen-frequencies between the baseline and optimised blades. The most critical change is the reduction in the separation between the second bending and first torsion modes of 66%.

The planform shape compared to the baseline and aeroelastic hover-optimised shapes in Figure 6. Including aeroelastic effects in blade optimisation requires adapting the blade's structural model The increase in blade twist, see Figure 7, and the advanced tip shape are apparent. The optimisation converges to the maximum available twist and shows a strong dihedral anhedral distribution in the final 10% of the span. The high twist and non-planar planform shape are the main drivers behind the improved performance. The optimised blade's surface pressure distribution shows a much more favourable behaviour as seen in Figure 8 . The high loading present at the blade tip near the leading edge for the baseline blade is completely removed for the optimised blade. The optimised blade

Table 5. Mode shape and corresponding eigen frequencies for the baseline and optimised blades

Mode Shape	Baseline Blade	Optimised Blade
Rigid Lag	2.31	2.24
Rigid Flap	4.66	4.65
First Bending	11.52	11.75
Second Bending	19.16	19.64
First Torsion	21.98	20.58
First Lag	24.41	23.76
Third Bending	29.21	30.77
Fourth Bending	42.76	43.62
Fifth Bending	58.98	59.10
Second Torsion	65.84	64.34

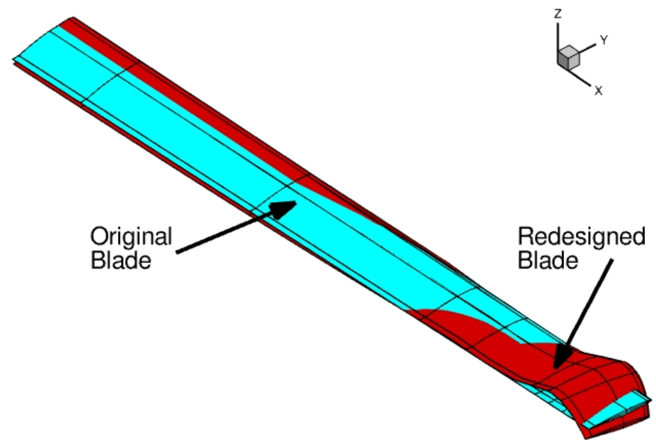

(a) Planform

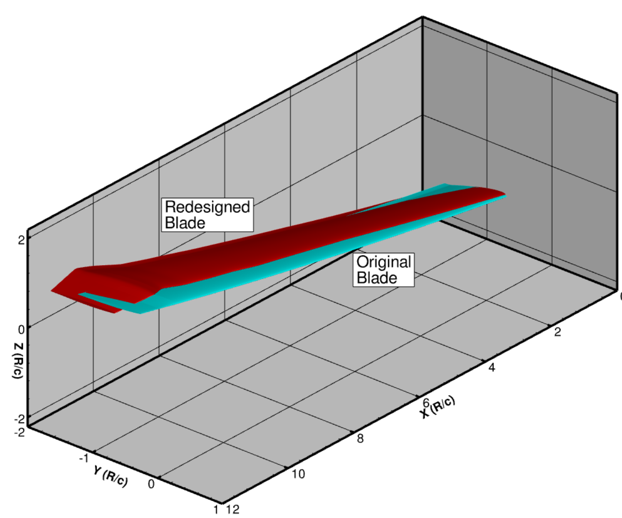

(b) Aeroelastic deflection at 6 degrees collective.

Figure 6. Base line and aeroelastic hover-optimised blade shapes.

significantly offloads the tip, with only a weak suction near the leading edge. The tip vortex field shows weaker tip vortices

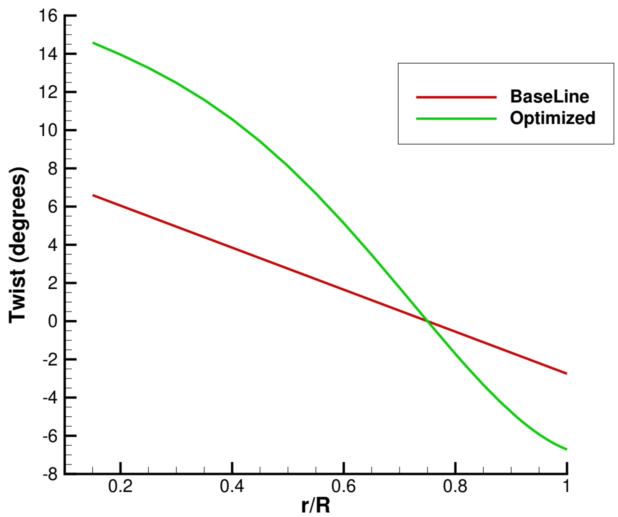

Figure 7. Base line and aeroelastic hover-optimised blade twist.

generated by the optimised blade design. The first tip vortex passage is barely visible for the optimised blade design. However, the blade sheds move complex vortex structures due to the sharp dihedral-anhedral distribution.

Figure 9 shows the figure of merit for the original and optimised blades, showing significant improvement. Some of the improvements are because the twist has now increased. Nevertheless, there is another very significant contribution: the clearance between the tip of the blade and the tip vortex shown in figure 10 for the case of a collective angle of 9.5 degrees.

Forward Flight Aeroelastic

The modal harmonic balance method was used to perform calculations for the baseline rotor blade. By looking at the displacement and velocity of the blade flapping mode, see figure 11, it can be seen that four harmonic balance modes are enough to adequately resolve the variation of modal amplitudes in time.

The hover optimised blade was also calculated to the same flight conditions of $C_T = 0.009$ with three different advanced ratios $\mu = 0.25$, $\mu = 0.3$, and $\mu = 0.35$. The results are shown in figure 12.

The forward flight test case uses the same parameterisation as the hover case. The thrust and torque sensitivities with respect to the design variables were calculated at three different advanced ratios, as shown in figure 13. At all advanced ratios, the sensitivities highlight that reducing the blade twist would be beneficial, and this benefit increases with advanced ratios. The sensitivities in chord, sweep and anhedral showed similar trends for the different advanced ratios. Reducing the chord in the tip region will see the most significant improvement in rotor forward flight performance. In the sweep, there appears to be a benefit in first sweeping backwards, then forwards, and

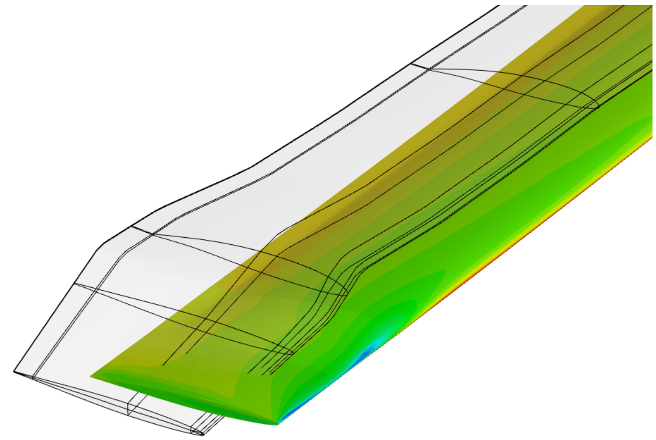

(a) Baseline at 6 degrees collective.

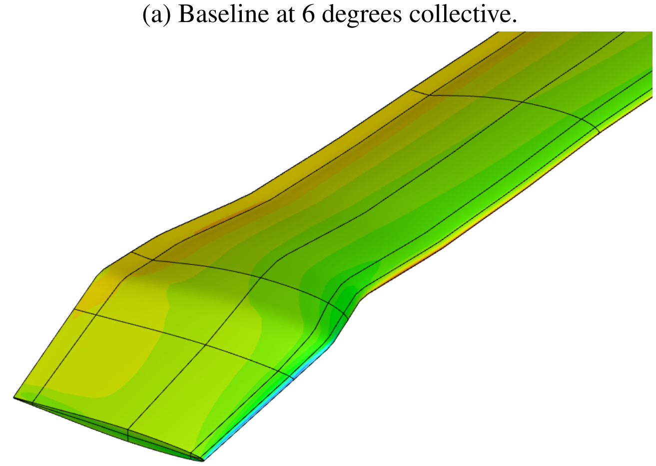

(b) Optimised blade at 6 degrees of collective.

Figure 8. Comparison of the original and optimised blades at the same collective.

finally backwards again. Decreasing the anhedral in the tip region will improve forward flight performance. These changes would all lead to a degradation in the hover performance.

CONCLUSIONS

The coupled adjoint, aeroelastic blade optimisation method built around the HMB3 flow solver was demonstrated here for hover and forward flight. The method is robust and efficient given the complexity of the problem, with the harmonic balance method helping to avoid time-marching computations, and with no dependency on the number of variables in the design parameterisation. Starting from a rectangular blade, the hover efficiency was increased by 15%of max FoM and this did not lead to penalties in forward flight.

The method is a realistic alternative to decoupled techniques based on meta models and offers a great framework for exploring the blade design space with no need for databases of results to be created and curve-fitted. In the future the method will be demonstrated for different initial blade designs to head off any possibility of strong dependency between initial and final blade shapes.

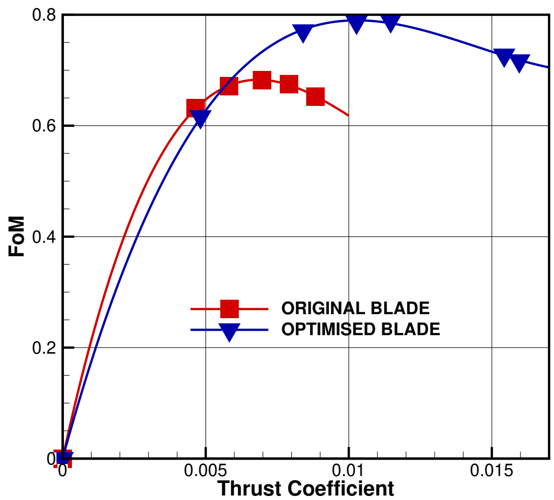

Figure 9. Comparison of the hover figure of merit between the original and optimised blades.

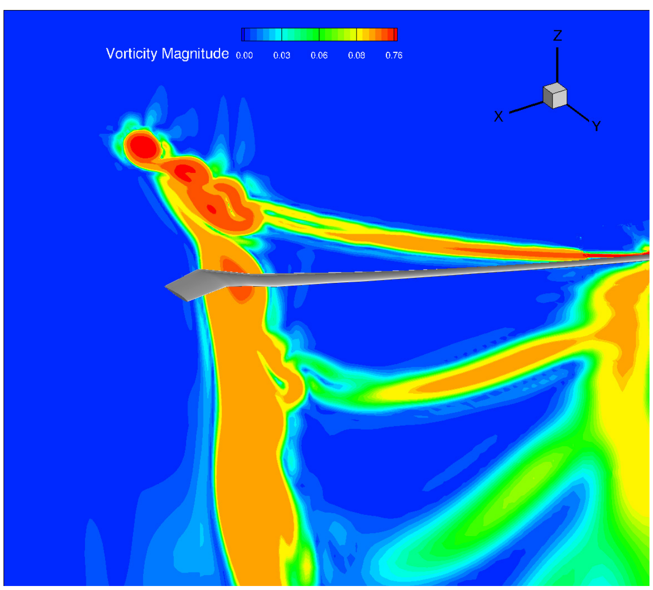

Figure 10. Flow visualisation using vorticity behind the hovering optimised blade ($\theta_{75} = 9.5$ degrees).

Author contact:
Mark A. Woodgate, mark.woodgate@glasgow.ac.uk,
George N. Barakos, george.barakos@glasgow.ac.uk.

ACKNOWLEDGMENTS

The sponsorship of the United States Army, Award Number: W911-NF-22-1-0083 is gratefully acknowledged. This work used the Cirrus UK National Tier-2 HPC Service at EPCC (http://www.cirrus.ac.uk) project ec004 and the ARCHER2 UK National Supercomputing Service (http://www.archer2.ac.uk) project e613.

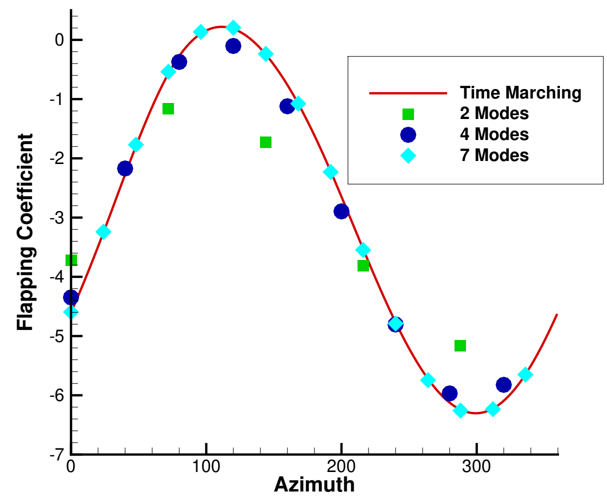

Figure 11. Convergence of the flapping coefficient with increasing number of harmonic balance modes.

REFERENCES

1. Robinson, K., and Brocklehurst, A., "BERP IV Aerodynamics, Performance and Flight Envelope," 34th European Rotorcraft Forum, 2008.

2. Rauch, P., Gervais, M., Cranga, P., Baud, A., Hirsch, J., Walter, A., and Beaumier, P., "Blue Edge^{TM}: The Design, Development and Testing of a New Blade Concept," 67th Annual Forum of the American Helicopter Society, 2011.

3. Behler, R. F., "Fiscal Year 2020 Director, Operational Test and Evaluation (DOT&E) Annual Report," https://www.dote.osd.mil/Portals/97/pub/reports/FY2020/other/2020DOTEAnnualReport.pdf, pp. 69-71 [Online; accessed 01-August-2023], 2021.

4. Fitzgibbon, T., *Advanced Rotor Blade Design based on High-Fidelity Computational Fluid Dynamics*, Ph.D. thesis, University of Glasgow, 2021.

5. Steijl, R., Barakos, G. N., and Badcock, K., "A framework for CFD analysis of helicopter rotors in hover and forward flight," *International Journal for Numerical Methods in Fluids*, Vol. 51, (8), DOI: 10.1002/d.1086, 2006, pp. 819–847.

6. Jarkowski, M., Woodgate, M., Barakos, G. N., and Rokicki, J., "Towards consistent hybrid overset mesh methods for rotorcraft CFD," *International Journal for Numerical Methods in Fluids*, Vol. 74, (8), DOI: 10.1002/fld.3861, 2014, pp. 543–576.

7. Osher, S., and Chakravarthy, S., "Upwind schemes and boundary conditions with applications to Euler equations in general geometries," *Journal of Computational Physics*, Vol. 50, (3), DOI: 10.1016/0021-9991(83)90106-7, 1983, pp. 447–481.

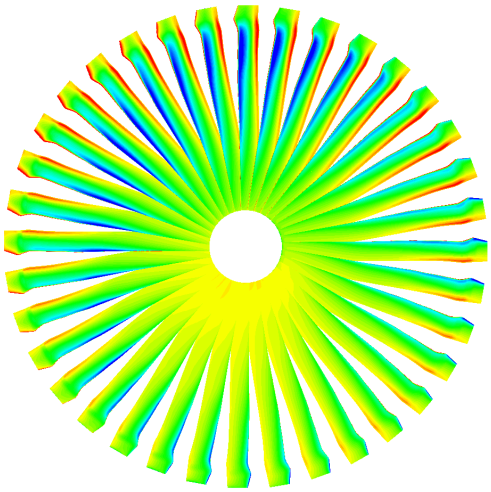

(a) $\mu = 0.25$

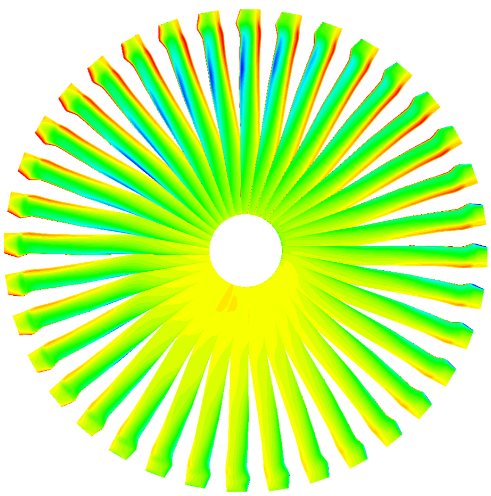

(b) $\mu = 0.30$

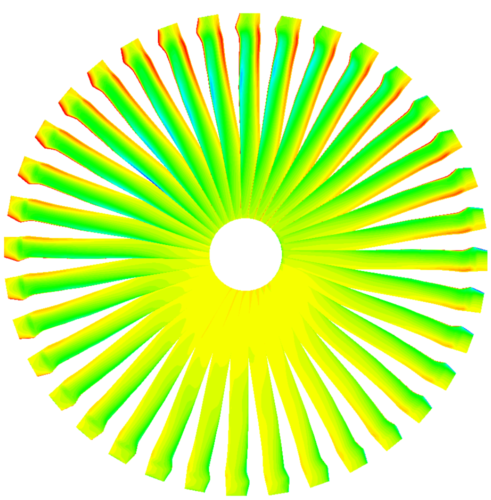

(c) $\mu = 0.35$

Figure 12. Comparison of pressure coefficient for the hover optimised blade at $C_T = 0.009$ and three different advance ratios $\mu = 0.25$, $\mu = 0.3$, and $\mu = 0.35$.

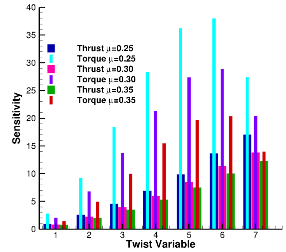

(a) Twist Variable

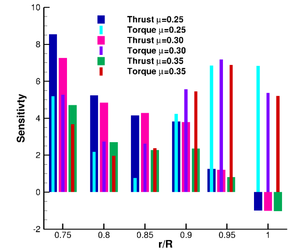

(b) Chord

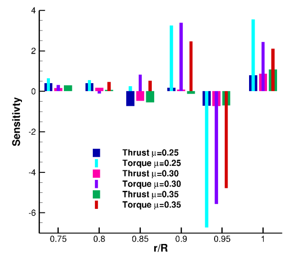

(c) Sweep

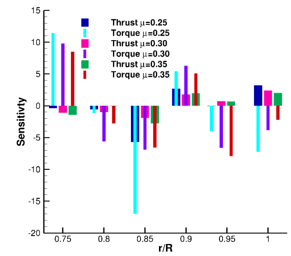

(d) Anhedral

Figure 13. Comparison of design sensitivities for the hover optimised blade at $C_T = 0.009$ and three different advance ratios $\mu = 0.25$, $\mu = 0.3$, and $\mu = 0.35$.

8. van Leer, B., "Towards the ultimate conservative difference scheme. V.A second-order sequel to Godunov's Method," *Journal of Computational Physics*, Vol. 32, (1), DOI: 10.1016/0021-9991(79)90145-1, 1979, pp. 101–136.

9. van Albada, G. D., van Leer, B., and Roberts, W. W., "A Comparative Study of Computational Methods in Cosmic Gas Dynamics," *Astronomy and Astrophysics*, Vol. 108, (1), DOI: 10.1007/978-3-642-60543-7, 1982, pp. 76–84.

10. Menter, F. R., "Two-Equation Eddy-Viscosity Turbulence Models for Engineering Applications," *AIAA Journal*, Vol. 32, (8), DOI: 10.2514/3.12149, 1994, pp. 1598–1605.

11. Ekici, K., Hall, K., and Dowell, E., "Computationally fast harmonic balance methods for unsteady aerodynamic predictions of helicopter rotors," *Journal of Computational Physics*, Vol. 227, (12), 2008, pp. 6206–6225.

12. Jameson, N. B. A., "Time Spectral Method for Rotorcraft Flow," 46th AIAA Aerospace Sciences Meeting and Exhibit, 2008.

13. Choi, S., and Datta, A., "Time-Spectral Method for CFD Prediction of Helicopter Rotor Vibratory Loads," 5th International Conference on CFD, 2008.

14. Woodgate, M., and Barakos, G., "Implicit Computational Fluid Dynamics Methods for Fast Analysis of Rotor Flows," *AIAA Journal*, Vol. 50, (6), 2012, pp. 1217–1244.

15. Hascoët, L., and Pascual, V., "The Tapenade Automatic Differentiation tool: Principles, Model, and Specifica-

tion," *ACM Transactions On Mathematical Software*, Vol. 39, (3), 2013.

16. Biava, M., Woodgate, M., and Barakos, G., "Fully Implicit Discrete-Adjoint Methods for Rotorcraft Applications," *AIAA Journal*, Vol. 54, (2), 2016, pp. 735–748.

17. Lancaster, P., and Salkauskas, K., "Surfaces generated by moving least squares methods," *Mathematics of computation*, Vol. 37, (155), 1981, pp. 141–158.

18. Luke, E., Collins, E., and Blades, E., "A fast mesh deformation method using explicit interpolation," *Journal of Computational Physics*, Vol. 231, (2), 2012, pp. 586–601. DOI: https://doi.org/10.1016/j.jcp.2011.09.021.

19. Wilkie, W., Mirick, P., and Langston, C., "Rotating Shake Test and Modal Analysis of a Model Helicopter Rotor Blade," Technical report, National Aeronautics and Space Administration, NASA TM-4760, 1997.

20. Choi, S., Lee, K., Potsdam, M., and Alonso, J., "Helicopter Rotor Design Using a Time-Spectral and Adjoint-Based Method," *Journal of Aircraft*, Vol. 51, (2), 2014, pp. 412–423.

21. Leon, E., Le Pape, A., Desideri, J., Alfano, D., and Costes, M., "Concurrent Aerodynamic Optimization of Rotor Blades Using a Nash Game Method," *Journal of the American Helicopter Society*, Vol. 61, (2), DOI: 10.4050/JAHS.61.022009, 2016, pp. 1–13.

22. Stanger, C., Hollands, M., Kessler, M., and Kramer, E., "Adaptation of the Dynamic Rotor Blade Modelling in CAMRAD for Fluid-Structure Coupling within a Blade Design Process." 18. DGLR- Fach-Symposium der STAB, 2012.

23. Wilke, G., "Applying Multi-Objective Variable-Fidelity Optimization Techniques to Industrial Scale Rotors: Blade Designs for CleanSky," 41st European Rotorcraft Forum, 2015.